

# CFD Analysis on Pipe Bend Flows

M.Shiva Kumar<sup>1</sup>, A. Mahaboob Basha<sup>2</sup>

<sup>1</sup>Dept of Mechanical Engineering

<sup>2</sup>Assistant Professor, Dept of Mechanical Engineering

<sup>1,2,3</sup> CRIT Engineering College, Anantapur

**Abstract-** One problem facing today's nuclear power industry is flow-accelerated corrosion and erosion in pipe elbows. The simulations are being performed using the FLUENT commercial software developed and marketed by Fluent, Inc. The model geometry and mesh were created using the ANSYS software, also from Fluent, Inc. This report documents the results of the simulations that have been made to date; baseline results employing the RNG  $k-\epsilon$  turbulence model are presented. The predicted value for the diametrical pressure coefficient is in reasonably good agreement with published correlations. Plots of the velocities, pressure field, wall shear stress, and turbulent kinetic energy adjacent to the wall are shown within the elbow section.

## I. INTRODUCTION

### BACKGROUND

The Korean Ministry of Science and Technology (MOST) and the U. S. Department of Energy (DOE) have teamed together through the International Nuclear Energy Research Initiative (INERI) to carry out a joint program of research into problems affecting the nuclear power industry. One such problem is flow-accelerated corrosion/erosion in pipe elbows. When fluid, in this case water, passes through a pipe elbow, the interaction between centrifugal and viscous forces creates a strong secondary flow in the plane normal to the pipe axis. This secondary flow consists of two counter-rotating vortices, one in either half of the pipe cross section. The scouring action of these vortices is believed to accelerate the processes of corrosion and erosion of the pipe wall; this in turn may lead to excessive vibrations, and possibly create a breach in the wall itself. The Korean Atomic Energy Research Institute (KAERI) is performing experiments in their Flow-Accelerated Corrosion (FAC) test loop to better characterize these phenomena, and develop advanced sensor technologies for the condition monitoring of critical elbows on a continuous basis. If successful, such monitoring can forewarn plant personnel of potential problems before they occur, thus avoiding unscheduled shutdowns which are very costly and intrusive.

### FLOW ACCELERATED CORROSION IN NUCLEAR POWER PLANTS

In general, corrosion is defined as the degradation of a material by means of chemical reactions with the surrounding environment. Several types of corrosion occur in a variety of situations in the nuclear power plants. Some of these types are common such as rusting of steel when located in moist environment, and the other type of corrosion such as flow accelerated corrosion required special treatment due to their impact on the plant safety and reliability. FAC degradation mechanism results in thinning of large areas of piping and fittings that can lead to sudden and sometimes to catastrophic failures, as well as a huge economic loss.

In general, erosion processes or mechanisms can be categorized as:

- i. Shear stress erosion
- ii. Liquid impact induced erosion
- iii. Flashing-induced erosion
- iv. Cavitation erosion

On the other hand, degradation mechanisms involve combined effect of chemical and mechanical processes can be summarized as:

- i. Erosion-corrosion: ii. Flow-Accelerated Corrosion: Furthermore, the repeated inspections in nuclear power plants have shown that piping components located downstream of flow singularities, such as sudden expansion or contractions, orifices, valves, tees and elbows are most susceptible to FAC damage. This is due to the severe changes in flow direction as well as the development of secondary flow instabilities downstream of these singularities. Moreover, in two-phase flows, the significant phase redistributions downstream of these singularities may aggravate the problem. Therefore, it is important to identify the main flow and geometrical parameters require in characterizing FAC damage downstream of pipe fittings. These parameters are: the geometrical configuration of the components, piping orientation, and the flow turbulence structure which will affect the surface shear stress and mass transfer coefficients.



Fig 1. Examples of failures due to FAC worldwide

## FLOW EFFECTS

The mass transfer coefficient primarily depends on flow. Physical properties of the diffusing species (in FAC it can be ferrous ions, oxygen, or other species participating in the reactions) affect MTC to a small degree. For a given species, the property effect depends on temperature as the physical properties such as the diffusion coefficient and viscosity depend on temperature. MTC correlations for a smooth wall have a velocity exponent of 0.8, while those for a rough wall have the velocity exponent changing from 0.8 for lower Reynolds numbers to 1.0 for very high Reynolds numbers<sup>2</sup>. In this context, smooth means hydrodynamic ally smooth: the surface asperities are smaller than the thickness of the laminar boundary layer; and rough means hydraulically rough with surface asperities higher than the thickness of the laminar boundary layer.

This change was gradual and took 3 days to reach steady state. It is possible that the velocity exponent is lower than 0.8, which occurs for cases where FAC rate is controlled partially or entirely by the mass transfer resistance of the oxide layer, or by the electrochemical reactions at the metal-oxide interface, or by both factors combined. If the velocity exponent is higher than 1, other effects are involved. In experiments of water with ammonia and pH about 9 in a pipe downstream of an orifice, Bignold report that the FAC rate depends on the MTC to the power of 3. They proposed an explanation that the velocity affects the electrochemical potential, which in turn, affects magnetite solubility. However, a significant majority of laboratory and plant data indicate a linear, or close to linear, relationship between the FAC rate and the flow velocity. Also, major computer codes for FAC rate calculations, CHECWORKS and BRT-CICERO, use the linear relationship. Changes in surface roughness resulting from FAC also can contribute to a non-linear relationship between the FAC rate and the MTC. At lower flow rates,

surface roughness may be weakly developed and at high flow rates, surface roughness may be fully developed. Other reasons for the reported nonlinearities are the calculations of the MTC from flow data, such as from the wall shear stress, instead of those obtained from mass transfer correlations. In some cases, empirical data on FAC rate are close to a linear relationship, and a reported square function fits the data only marginally better than a linear approximation.

## FLOW-ACCELERATED CORROSION IN BENDS

The role of flow in bends is discussed below as an illustration of the more general considerations aforementioned. Also, bends are the most typical component of piping and they frequently fail or have to be replaced because of excessive wall degradation.

### Mass Transfer Coefficient

For bends, the MTC can be calculated from an empirical correlation obtained directly for bends or from a bend geometry factor. For the latter, which is presented below, one needs also an MTC correlation for the straight pipe. Therefore, the MTC for the straight pipe is presented first. A majority of published correlations for a straight pipe are valid for low Reynolds numbers because it is expensive to conduct laboratory experiments under high Reynolds numbers (i.e., under high flow rates and high temperatures). Popular examples of these correlations for fully developed profiles are the Colburn and Dittus-Boelter correlation and the Berger and Hau correlation [9], which can be applied for a Reynolds number of tens of and hundreds of thousands.

### Local Distribution of MTC and FAC Rate

Two examples of local FAC rate distribution and a comparison with MTC results for CANDU outlet feeders are given below. In the examples, detailed measurements of plant specimens were made and CFD simulations of the MTC for each case were performed. In the first example, a short-radius bend with the ratio of bend radius to nominal pipe diameter equal to 1.5 is analysed. For details of the bend geometry, flow, and other parameters, see Table 1. The bend is located downstream of a sudden turn from the end fitting at the outlet from the reactor, which increases turbulence level significantly; therefore, profiles of velocity and concentration at the entrance of the bend are not fully developed.

## II. INTRODUCTION TO SOFTWARES USED

### INTRODUCTION OF ANSYS

ANSYS is general-purpose finite element analysis (FEA) software package. Nowadays, ANSYS package is playing an important role in all fields. The analysis capabilities of ANSYS include the ability to solve static and dynamic structural analysis, steady state and transient heat transfer problems, mode-frequency and buckling Eigen value problems and various types of field and coupled-field applications.

ANSYS Workbench, developed by ANSYS Inc., USA, is a Computer Aided Finite Element Modeling and Finite Element Analysis tool. In the Graphical User Interface (GUI) of ANSYS Workbench, the user can generate 3-dimensional and FEA models, perform analysis, and generate results of analysis and also it can be used to perform a variety of tasks ranging from Design Assessment to Finite Element Analysis to complete Product Optimization Analysis by using ANSYS Workbench.

## INTRODUCTION TO FLUENT

FLUENT is a state-of-the-art computer program for modeling fluid flow and heat transfer in complex geometries. FLUENT provides complete mesh flexibility, including the ability to solve your flow problems using unstructured meshes that can be generated about complex geometries with relative ease. Supported mesh types include 2D triangular/quadrilateral, 3D tetrahedral/hexahedral/pyramid/wedge/polyhedral, and mixed (hybrid) meshes. FLUENT also allows you to refine or coarsen your grid based on the flow solution. FLUENT is written in the C computer language and makes full use of the flexibility and power offered by the language.

Consequently, true dynamic memory allocation, efficient data structures, and flexible solver control are all possible. In addition, FLUENT uses a client/server architecture, which allows it to run as separate simultaneous processes on client desktop workstations and powerful compute servers. This architecture allows for efficient execution, interactive control, and complete flexibility between different types of machines or operating systems. All functions required to compute a solution and display the results are accessible in FLUENT through an interactive, menu-driven interface.

## III. MODEL GEOMETRY AND MESH

Figure 2 shows a plan view of the pipe elbow geometry used in the fluid simulations (note that the figure is not drawn to scale). The  $(x,y)$  coordinates are in the plane of the paper, with the origin centered at the pipe inlet in the lower

left corner;  $z$  is positive out of the paper. The pipe has an inside diameter  $D = 35.5$  mm. Flow enters a straight section 200 mm long at the lower left corner of the figure. This is followed by a 90° elbow section, and then another straight section of pipe 350 mm in length. The downstream leg also contains a representation of the chemical sensor used in the experiments, and its support bracket. The sensor itself is modelled as a circular cylinder 6.4 mm in diameter, mounted concentrically within the pipe. The support bracket is assumed to span the pipe horizontally, with a vertical height of 8.4 mm; it has a thickness of 3 mm. The sensor protrudes 10 mm upstream of the bracket, and is also assumed to extend all the way to the outlet from the model as shown at the top of the figure. Thus the outlet cross section is the annular space between the cylindrical sensor and the pipe wall.

In the actual FAC test loop, there is a “tee” in the pipe where we have assumed our outlet to be. Including the tee in our model would have required that we also include a significant length of pipe downstream of the tee as well, to give the flow time to readjust to a condition where a uniform outlet boundary condition could reasonably be applied. This would result in a much larger model, a more complex and time-consuming meshing exercise, and a greatly increased number of mesh cells. Moreover, the tee is sufficiently far downstream that its presence should not have an appreciable influence on the flow in the elbow. It can certainly be expected to have less influence than the chemical sensor and its bracket. For these reasons, it was decided not to include the tee, but rather to simply end the straight section downstream of the elbow where the tee would have been, with the inner cylinder representing the sensor extending all the way to the outlet.

Fig. 3 shows a cross-sectional view of the mesh in the portion of the model upstream of the chemical sensor. Note that the mesh is greatly refined in the vicinity of the pipe wall, in order to capture the large gradients in the viscous boundary layer. The cell immediately adjacent to the wall is specified to have a thickness of 0.15 mm; the cell thickness then gradually increases with distance from the wall. This was accomplished by attaching what GAMBIT refers to as a Boundary Layer Mesh to the pipe wall. The mesh outside the boundary layer was created by paving the remaining area with quadrilateral elements with a nominal size of 0.5 mm. This 2D surface mesh was ‘swept’ along the axis of the pipe to generate a volume mesh of hexagonal cells.

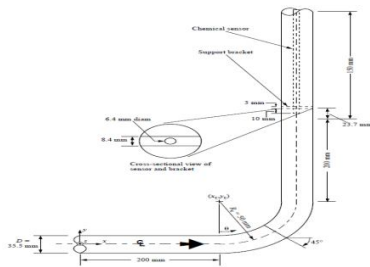


Fig 2. Pipe Elbow Model Geometry (not to scale)

The mesh in the annular portion of the pipe with the sensor present (not shown here) is very similar to that in Fig. 3, except that the volume occupied by the sensor and its bracket is no longer available to the flow. Hence it has a circular cut-out on the axis (the projection of the sensor cylindrical face) within which no elements are present. No attempt was made to resolve the boundary layers adjacent to the sensor and support bracket, as such details are not of immediate interest to the current project. Nevertheless, the primary effect of the sensor and bracket on the flow in the vicinity of the pipe elbow, which is to reduce the portion of the cross sectional area that is available to the flow, is still adequately accounted for in the solutions. This mesh is also swept along the axis, and is essentially preserved throughout the portion of pipe containing the sensor.

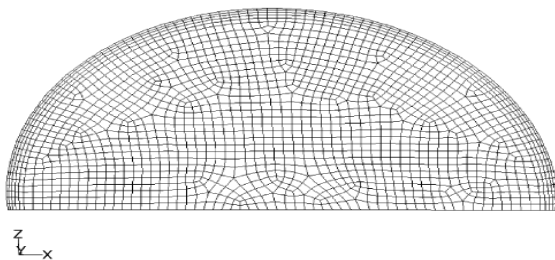


Fig 3. Cross-sectional View of Mesh Upstream of Chemical Sensor

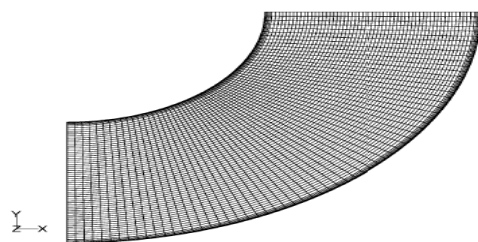


Fig. 4. Top View of Mesh on the Elbow Symmetry Plane

Fig. 4 shows the mesh on the floor (symmetry plane) of the elbow section. Again, the Boundary Layer Mesh applied to the outer wall is evident along both the inner and outer radii. The cell dimension in the stream wise direction varies between ~ 0.5 - 1.2 mm along the inner radius and 1.4 - 1.8 mm along the outer radius, depending on distance from the

center of the arc. Though not shown here, stream wise cell dimensions of this order are also used in the immediate vicinity of the leading edge of the sensor and its support bracket to resolve the larger stream wise gradients expected there. Away from these two regions the stream wise cell spacing is gradually increased to reflect the fact that the flow is expected to be more uniform. Thus, near the inlet,  $\Delta x$  for a cell is ~ 10 mm, while at the outlet, the cell  $\Delta y$  is ~ 5 mm. The resulting volume mesh for the entire model contains a total of 514,043 hexagonal cells, and 540,144 nodes.

**FLOW MODEL**

The problem is treated as the steady flow of a viscous, incompressible (*i.e.*, constant density), and isothermal liquid, with the working fluid being water. Gravitational effects are ignored. The specified temperature is  $T = 90^\circ\text{C}$  ( $200^\circ\text{F}$ ), for which the density and viscosity of water are  $\rho = 965.35 \text{ kg/m}^3$ , and  $\mu = 3.145 \times 10^{-4} \text{ kg/(m}\cdot\text{sec)}$  (p. 6-3). The flow velocity at the inlet, as averaged over the pipe cross section, is assumed to be  $U_{avg} = 5 \text{ m/sec}$ . This results in a Reynolds number of which indicates that the flow can be expected to be fully turbulent. Though turbulent flows are inherently unsteady, it is the prediction of the mean, or averaged, properties of the flow that is typically of most interest. For this purpose, it is necessary to augment the underlying flow equations by a turbulence model, which is discussed next.

$$Re = \frac{\rho U_{avg} D}{\mu} \approx 5.4 \cdot 10^5 \tag{1}$$

**Turbulence Model**

The flow considered here, as with many flows of engineering interest, can be viewed as a steady mean flow on which is superimposed a fluctuating turbulent field, *i.e.*,

$$u = \bar{u} + u' \quad v = \bar{v} + v' \quad w = \bar{w} + w' \tag{2}$$

where  $(\bar{u}, \bar{v}, \bar{w})$  are the mean components of the local fluid velocity along  $(x, y, z)$  respectively, and the overbar  $(\bar{\dots})$  denotes a time-average. The  $(u', v', w')$  represent the turbulent components, which by inference have zero mean value. When Eq. (2) is substituted into the Navier-Stokes equations of motion, and the result averaged over time, the resulting system of equations involves not only  $(\bar{u}, \bar{v}, \bar{w})$ , but also quantities such as  $\overline{u'^2}, \overline{v'^2}$  as well as cross products like  $\overline{u'v'}, \overline{v'w'}$  etc. These are commonly referred to as the Reynolds-Averaged Navier-Stokes (RANS) equations. Their solution is

problematic, in that the number of unknowns—which now include the primed (turbulent) quantities—exceeds the number of equations.

To achieve closure, recourse is made to a *turbulence model*. A turbulence model, based on a combination of heuristic argument and empirical knowledge, supplies the needed additional equations that relate the primed quantities to the mean flow variables. One of the most widely used turbulence models is the two-equation  $k$ - $\varepsilon$  model developed by Launder and Spalding, so named because it introduces an additional pair of partial-differential equations for predicting the turbulent kinetic energy per unit mass,  $k$ , and its rate of dissipation,  $\varepsilon$ . The model incorporates several constants whose values have been determined from experiments with both air and water for fundamental turbulent shear flows. It has been found to work fairly well for a wide range of wall-bounded and free shear flows.

$$k = \frac{1}{2}(\overline{u'^2} + \overline{v'^2} + \overline{w'^2}) \quad (3)$$

A later model uses a more rigorous statistical technique known as “ReNormalization Group” (RNG) theory. Similar in form to the standard  $k$ - $\varepsilon$  model above, it results in an analytical derivation of the values of the model constants, which differ from those in the standard model. In addition, new terms are introduced in the transport equations for  $k$  and  $\varepsilon$  that, among other things, allow them to more accurately compute turbulent flows involving swirl. The reduced dependence on empiricism, and the inclusion of the additional terms make this so-called RNG  $k$ - $\varepsilon$  model more accurate and reliable for a wider class of flows than the standard  $k$ - $\varepsilon$  model. For these reasons it was chosen for use in the present simulations. Rather than try to fully resolve the viscous sublayer and the buffer layer that underlie the fully turbulent portion of the boundary layer adjacent to solid surfaces, wall functions were employed. Non equilibrium wall functions, as opposed to the standard wall function treatment, were used because of their ability to include the effects of pressure gradients and strong non-equilibrium; as a result improved predictions of wall shear stress, among other things, can be obtained.

### Solution Algorithm

The Navier-Stokes equations, which express the conservation of mass and momentum, and the transport equations for  $k$  and  $\varepsilon$  used in the turbulence model, form a coupled set of nonlinear partial-differential equations (PDEs). FLUENT uses a finite-volume discretization to convert the

PDEs to a set of nonlinear algebraic equations. The solutions obtained here employ the segregated solution algorithm, in which the equations are solved sequentially, as opposed to being assembled into a single matrix equation and solved simultaneously. Since the equations are nonlinear and coupled, the segregated method requires that an iterative process be used: starting from an initial “guess” for all the variables, the solution is updated, or allowed to “relax”, toward the final steady-state solution as the iterations proceed.

To obtain a unique solution to the system of equations for the mean velocity ( $\bar{u}$ ,  $\bar{v}$ ,  $\bar{w}$ ) and pressure,  $\bar{P}$  one must supply boundary conditions on all surfaces bounding the flow. Furthermore, since an iterative technique is used by FLUENT, a set of initial conditions for all the flow variables must also be supplied to start the iterations.

### Boundary Conditions

The surfaces bordering the fluid domain fall into one of four categories: 1) the symmetry plane; 2) the planar surface at  $x = 0$  where the water enters the domain in the lower left corner of Fig. 4.1, referred to simply as the inlet; 3) the solid walls representing the pipe, chemical sensor, and associated bracket; and 4) the planar surface at  $y = 400$  mm where the water exits the domain. The latter three require that additional information be supplied, as described below.

#### Symmetry Plane

This is the portion of the  $z = 0$  surface that lies within the pipe. Here the boundary condition is  $w = 0$ , and  $\partial(\dots)/\partial n|_{z=0} = 0$  for all flow variables, as discussed previously. No user-specified values are supplied at a symmetry plane.

#### Inlet

At the inlet to the domain at  $x = 0$  we apply what FLUENT terms a VELOCITY INLET boundary condition, *i.e.*, the three components of velocity are specified. The simplest assumption would be to set the axial velocity everywhere in the pipe equal to its average value,  $U_{avg} = 5$  m/sec. However, such a “plug flow” is unrealistic because it does not satisfy the noslip boundary condition at the pipe wall, which the real flow must meet. Moreover, the length of pipe required for the flow to adjust from a uniform inflow to a profile that is no longer a function of distance from the inlet—the so-called “inlet length”,  $L_I$ —can be several pipe diameters long. Blevins, in his Eqn. (6-5), gives the following empirical relation in terms of  $Re$  for turbulent flows:

$$L_1/D = 14.21 \log_{10} Re - 46 \quad \text{for } Re > 10,000 \quad (4)$$

For the current case with  $Re = 5.4 \times 10^5$ , this indicates an inlet length of 35 diameters. Extending the straight section ahead of the elbow by this much would have greatly increased the size of the model, the number of cells, and the computational requirements. Instead, FLUENT’s ability to accept boundary profile data was used; that is, instead of a uniform plug flow, a nonuniform tabulated profile for the axial velocity vs. radius,  $u(r)$ , was specified.

$$\frac{n}{U_c} = \left(\frac{R-r}{R}\right)^{1/n} \quad n = f^{-1/2} \quad (5)$$

$$\frac{U_c}{U_{avg}} = \frac{(n+1)(2n+1)}{2n^2}$$

where  $U_c$  is the velocity at the centerline,  $r = 0$ , and  $f$  is a nondimensional “friction factor” which in general depends on both  $Re$  and the wall roughness,  $\bar{u}(r)$ . The pipe material was assumed to be carbon steel; from Table 6-4 in Blevins, a surface roughness of  $\epsilon_r = 0.1$  mm was assumed, and  $f$  computed from Blevins’ Eq. (6-12),

$$f = \left[ 1.14 - 2 \log_{10} \left( \frac{\epsilon_r}{D} + \frac{21.25}{Re^{0.9}} \right) \right]^{-2} \quad (6)$$

which yields  $f = 0.026$ . The normalized profile of  $u/U_c$  vs.  $r/R$ , where  $R$  is the pipe radius, is plotted in Fig. 4. It should be emphasized that this profile is *not* applied throughout the flow; it is only used as a boundary condition at the inlet plane to avoid having to use a much larger model. The other mean velocity components,  $v$  and  $w$ , are set to zero at the inlet. The turbulence intensity of the incoming flow was specified from the empirical relation given by Eq. (6.2-1).

$$I \equiv \frac{\sqrt{\frac{2}{3}k}}{U_{avg}} \equiv \frac{0.16}{Re^{1/8}} \quad (7)$$

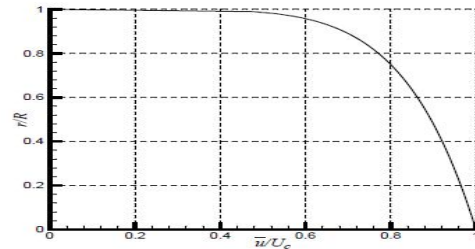


Figure 5. Profile of Axial Velocity for Fully-Developed Turbulent Pipe Flow

which gives  $I = 3\%$ . Since the pipe’s cross section is circular, its hydraulic diameter is assumed equal to its geometric diameter,  $D = 35.5$  mm. These quantities are used internally by FLUENT to specify values for the turbulence variables at the inlet.

### Walls

For an impenetrable wall, there can be no flow normal to its surface, and since we are also treating the flow as viscous, the velocity components tangential to the wall must vanish there as well. This is the “no-slip” boundary condition, for which all three components of velocity are identically zero at the wall. This condition was used for both the pipe wall, and the surfaces representing the chemical sensor and its support bracket.

In addition, the wall roughness must be specified. As noted above, the pipe wall is assumed to be carbon steel, with  $\epsilon_r = 0.1$  mm. The chemical sensor and its bracket, however, are assumed to be made of more highly polished material, for which it was assumed  $\epsilon_r = 0$ . This does not mean that the shear stress at their surface is zero, but only that it is less than would be the case if  $\epsilon_r > 0$ . This assumption is justified by the fact that the biggest effect of the sensor/bracket on the flow in the elbow is likely to be due to their blockage of the cross section that is available to the flow, and not the viscous drag they exert on it; this is confirmed in §4 where the numerical results are discussed. It is also consistent with the decision to not resolve the boundary layers on the sensor cylindrical wall and the surfaces of its support bracket (*cf.* §2).

### Outlet

At the outlet at  $y = 400$  mm in Fig. 4.1, FLUENT’s PRESSURE OUTLET boundary condition is applied. This requires that a value for the gauge static pressure be provided, as well as the turbulence properties. For  $p$ , a gauge pressure of 19 bar (absolute pressure of 20 bar), which is representative of the KAERI experiments, was specified. The option of using a radial equilibrium pressure distribution was chosen to account for any residual secondary flow that may be present at the

outlet. (The meaning of this is discussed in more detail in §4.2 below.)

**Initial Conditions**

Before the iterations toward a steady-state solution can begin, each of the variables at every cell must be given an initial value. Even though the converged steady-state solution should be independent of the assumed initial conditions, some care is advisable in choosing them. The closer they are to the final solution, the faster and more easily will the iterations converge; conversely, a bad initial guess may prevent convergence altogether.

For present purposes, constant values were used throughout the mesh:  $(\bar{u}, \bar{v}, \bar{w})$  are set to (0,0,0) in all cells and the starting gauge pressure was set to 19.1 bar everywhere—*i.e.*, 0.1 bar higher than the pressure at the outlet. The initial values for  $k$  and  $\epsilon$  were  $0.0345 \text{ m}^2/\text{sec}^3$  and  $0.419 \text{ m}^2/\text{sec}^3$ , respectively. The latter were computed internally by FLUENT as average values over the inlet plane, based on the turbulence parameters specified there in §3.3.

**IV. RESULTS**

The residuals in the governing equations had all fallen below  $10^{-4}$  after a total of 3200 iterations had been performed, at which point the solution was considered converged. In addition to monitoring the residuals, the mass flow rate at the outlet was computed every couple of hundred iterations and compared to the (specified) mass flow rate at the inlet, 2.379 kg/sec. At convergence, the two differed by less than  $3 \times 10^{-6}$ .

The focus here is primarily on conditions in the elbow, as that is where the accelerated corrosion/erosion takes place. To illustrate the nature of the secondary flow, Fig. 6 shows the two-dimensional in-plane velocity vectors in the cross-section normal to the center line at the midpoint of the elbow, *i.e.*, the 45° plane marked in Fig. 2. The perspective is that of an observer upstream of the plane looking at it head-on, with the inner radius on the left and the outer radius on the right. The length and orientation of each vector are determined by the magnitude and direction of the in-plane velocity characterizing the secondary flow. In addition, each vector is color-coded according to the magnitude of the full three-dimensional velocity, as shown by the color bar. As described above, only the solution in the top half of the pipe was computed; the results in the bottom half were obtained by reflecting about the symmetry plane. Also, to minimize the visual clutter created by overlapping vectors, only every third vector has been plotted in Fig. 6.

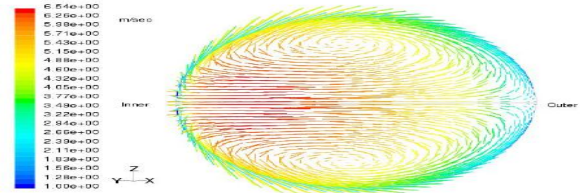


Fig 6. Two-Dimensional In-Plane Velocity Vectors at Elbow Midsection, Colored by Three-Dimensional Velocity Magnitude

When flow enters the elbow section, the faster moving portion near the axis (*cf.* Fig. 5) gets displaced outward from the centerline due to inertial effects, resulting in a general migration from the inner toward the outer radius of the bend. The fluid then enters the viscous boundary layer on the outer wall (the region of relatively slow velocity in blue and green), where it is transported back toward the inner radius, completing the loop. Thus the secondary flow consists of two vortical flows of opposite sign: a counter clockwise circulation in the top half, accompanied by a clockwise circulation in the bottom half. When the axial component of the flow is added to these in-plane vectors, the resultant pathlines followed by the fluid particles are helical.

Contours of absolute pressure at the elbow midsection are displayed in Fig. 7; from here on, only the top half of the cross section is shown. The fact that the contours are nearly vertical and evenly-spaced over much of the interior means that the pressure gradient is primarily in the horizontal direction, and nearly constant in magnitude. It is this horizontal gradient that is ultimately responsible for keeping the flow turned along the axis of the pipe. Blevins discusses the so-called *diametrical pressure coefficient*,  $ck$ . This quantity is defined as:

$$c_k = \frac{\bar{P}_o - \bar{P}_i}{\frac{1}{2} \rho U_{avg}^2} \tag{8}$$

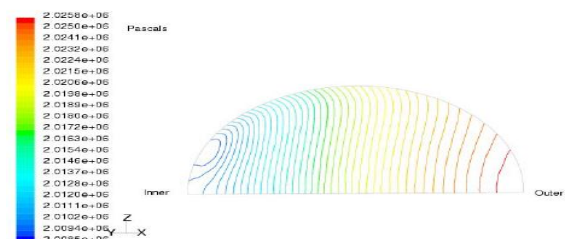


Figure 7. Contours of Absolute Pressure at Elbow Midsection

where  $\bar{P}_o$  and  $\bar{P}_i$  are the pressures where the outer and inner radii of the bend intersect the symmetry plane, respectively.  $ck$  is ordinarily measured at that station where

the flow has gone through one-half the total bend angle, *i.e.*, in this case the 45° section shown in Fig. 7. The FLUENT simulation predicts  $\bar{P}_o - \bar{P}_i = 16,370$  Pa, yielding  $c_k = 1.36$ . For the range of *Re* of interest here, the experimental data are correlated by the expression,

$$c_k \cong \frac{2D}{R_c} \quad Re > 5 \times 10^5 \quad (9)$$

which gives the value 1.42. This is considered reasonably good agreement in view of the fact that the data on which Eq. (9) is based were obtained for gentle bends,  $Rc/D > 2$ . For sharper bends such as the present case,  $Rc/D = 1.41$ , Blevins notes that the data show considerable scatter.

The generally higher pressures on the outer radius are also evident in Fig. 8, which shows contours of constant absolute pressure on the pipe wall of the elbow section. The first view is the same as in Fig. 2, *i.e.*, looking directly down on the elbow along the -z direction. The second view is from the perspective of an observer looking up into the interior of the pipe from below the symmetry plane, with the inner radius in the distance, and the outer radius closer to the observer, as indicated. To accentuate the variations in this region, the maximum and minimum values on the color bar have been chosen based solely on the values in the elbow, not on those for the entire model; unless stated otherwise, it can be assumed that this is also the case for subsequent plots as well. In addition to the transverse pressure gradient, a general decrease in pressure in the stream wise direction is also evident. More will be said on this point later.

It was believed that flow-accelerated corrosion/erosion would be most evident in areas of high wall shear stress. Accordingly, Fig. 9 presents a contour plot of the shear stress on the pipe wall of the elbow section. Surprisingly, the results indicate that the maximum wall shear occurs not on the outer radius, but on the inner radius near the entrance to the elbow. Along the inner radius, the wall shear decreases from its maximum more or less monotonically from the entrance to the exit of the elbow section; the opposite trend holds true along the outer radius. If true, these results suggest that either: a) the maximum corrosion/erosion should be expected along the inner radius of the pipe, not the outer radius as was expected; or, b) if corrosion is found predominantly on the outer radius, some mechanism other than the purely fluidmechanical scouring of the pipe surface is responsible.

The wall shear stress is the product of the molecular viscosity  $\mu$  and the gradient normal to the wall of the local

fluid velocity. The latter is dominated by the radial gradient of the axial velocity component,  $\partial \bar{u}_a / \partial r$ . The axial velocity,  $\bar{u}_a$ , is the component parallel to the pipe axis at each station. FLUENT however, obtains its solution in terms of the cartesian components  $(\bar{u}, \bar{v}, \bar{w})$ . For any location within the elbow,  $\bar{u}_a$  can be computed from the Cartesian components as follows,

$$\bar{u}_a = \bar{u} \cos \theta + \bar{v} \sin \theta \quad (10)$$

where  $\theta$  denotes the azimuthal angle in the (x, y) plane measured counterclockwise from the beginning of the elbow section, as shown in Fig. 2

:

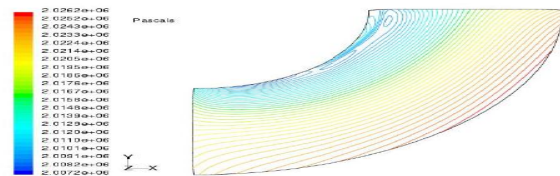


Fig 8 Contours of Absolute Pressure on Wall in Elbow Section; top view

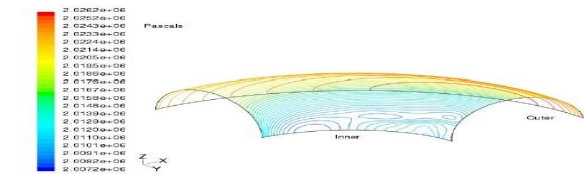


Fig 8. Contours of Absolute Pressure in Elbow Section; inside view (concluded)

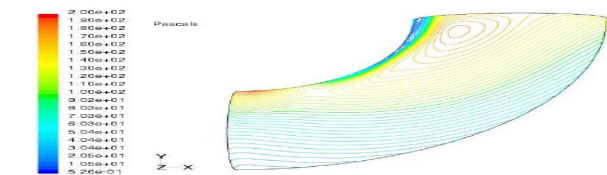


Fig 9. Contours of Wall Shear Stress on Pipe Elbow, top view

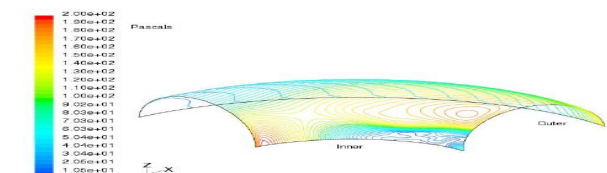


Fig 9. Contours of Wall Shear Stress on Pipe Elbow, inside view (concluded)

$$\theta = \sin^{-1} \frac{x - x_c}{[(x - x_c)^2 + (y - y_c)^2]^{1/2}} \quad \text{for } x \geq x_c \text{ and } y \leq y_c \quad (11)$$



Note that at the entrance to the elbow,  $\theta = 0^\circ$  and Eq. (10) reduces to  $\bar{u}_a = \bar{u}$ , while at its exit  $\theta = 90^\circ$  and  $\bar{u}_a = \bar{v}$ , as it should.

Equations (10) and (11) were used within FLUENT to define  $\theta$  and  $\bar{u}_a$  in terms of the intrinsic variables  $x, y, \bar{u}$ , and  $\bar{v}$ , and the constants  $x_c$  and  $y_c$ , using its Custom Field Function capability. This allows contours of  $\bar{u}_a$  to be plotted as with any other variable. Figures 10-12 show contour plots of  $\bar{u}_a$  over the pipe cross section at the beginning, the midway section, and the end of the elbow, respectively. The same minimum and maximum values on the color bars have been used for all three plots to facilitate comparisons. At the elbow entrance in Fig. 10, it is clear that the faster moving fluid starts out displaced towards the inner radius. That, coupled with the tighter spacing of the contours in that region, results in the wall shear taking on its maximum value there (cf. Fig. 9).

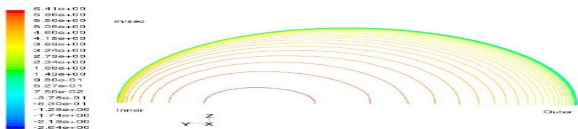


Fig 5.5. Contours of Axial Velocity at Beginning of Elbow,  $\theta = 0^\circ$

Fig. 5.6 shows the axial velocity contours at the elbow midsection,  $\theta = 45^\circ$ . This is the same cross section viewed in Fig. 6, except there it was the in-plane velocity vectors that were displayed. The axial velocity field shown in Fig. 11 can be thought of as the out-of-plane component. The faster-moving fluid is still hugging the inner radius as it did in Fig. 10. (This is also evident in Fig. 6, where the vectors are color-coded according to the magnitude of the full three-dimensional velocity vector.) However, the thickness of the relatively slow moving boundary layer on the inner wall (the blue and green contours) has increased significantly. This means an increased spacing between the contours, or a reduced wall shear stress, consistent with Fig. 9.

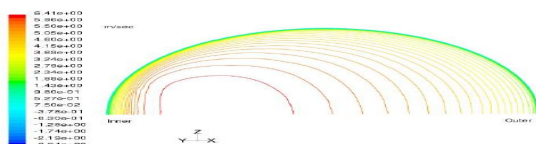


Fig 11. Contours of Axial Velocity at Elbow Midsection,  $\theta = 45^\circ$

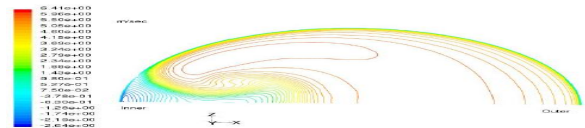


Figure 12. Contours of Axial Velocity at End of Elbow,  $\theta = 90^\circ$

Finally, the axial velocity contours at the end of the elbow,  $\theta = 90^\circ$ , are displayed in Fig. 12. The most notable feature of this plot is that the faster moving fluid has been displaced upwards, towards the top of the pipe. (In the bottom half, not shown here, the faster moving fluid is displaced toward the bottom of the pipe.) This is accompanied by a tightening of the spacing between contours in this region, consistent with the local maximum in shear stress exhibited in Fig. 9. Equally interesting is the region near the intersection of the inner radius and the symmetry plane, where significant negative axial velocities, i.e., backflow, is predicted. This is typically the result of the main flow having separated from the surface.

That this is indeed what happens can be seen from Fig. 13, which displays the in-plane velocity vectors in the plane of symmetry, color-coded according to the velocity magnitude. Note that, because this is the symmetry plane, the out-of-plane component  $w$ , the  $z$ -component of velocity, is identically zero. Thus the vectors shown are in fact the total vectors, and the two and three-dimensional vector magnitudes are one and the same. Also note that the scale on the mapping a particular velocity component, which may be either positive or negative; but that in Fig. 13 maps the velocity magnitude, which is by definition always positive. To reduce the visual clutter created by overlapping vectors, again only every third vector has been drawn.

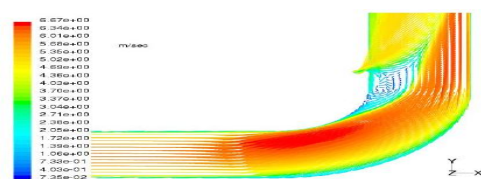


Fig 13. Two-Dimensional In-Plane Velocity Vectors in Plane of Symmetry, Colored by Velocity Magnitude

Fig. 13 clearly shows the fast moving fluid near the elbow entrance tends to hug the inner pipe wall (cf. Fig. 10), but is displaced outward as it passes through the elbow. Just downstream of the  $45^\circ$  midsection, the flow separates from the inner radius, and a large separation bubble is formed that extends a good distance downstream. There is a significant counter-clockwise recirculation within the bubble, its center being located near the elbow exit. Thus fluid to the right of this center has a positive axial flow component, while the

relatively thin layer between it and the inner wall has a negative axial velocity, albeit rather small. This is consistent with the picture presented in Fig. 12.

It is not known whether such separation occurs in the experiments or not, as no measurements of the velocity field were made, nor was any flow visualization performed. If indeed present, it can certainly be expected to have a major impact on the character of the flow, and where the maximum wall shear stress will occur. The flow will be more likely to separate as the ratio  $Rc/R$  approaches one (corresponding to a quarter-section of a “donut” with a vanishingly small hole), and less likely to separate as this ratio increases ( $Rc/R \rightarrow \infty$  corresponding to a straight pipe). The author is unaware of any field data indicating whether the degree of pipe elbow corrosion/erosion correlates with this ratio or not.

Conceivably, some measure of the turbulence level itself might correlate better with corrosion and erosion than the wall shear stress. Figure 13 displays contours of constant turbulent kinetic energy, as defined in Eq. (3), on the elbow wall. Actually, because of the no slip boundary condition,  $(u', v', w')$  must all vanish right at the wall; hence  $k$  will also be zero there. What is actually plotted in Fig. 14 is the turbulent kinetic energy in the first cell off the wall surface. As was the case with wall shear stress, the maximum occurs on the inside radius just downstream of the elbow entrance. Hence it appears doubtful that a mechanism related to turbulence would result in maximum corrosion on the outer radius.

**Influence of Turbulence Model**

For the reasons stated in §3.1, the above results were all obtained using the RNG  $k-\epsilon$  turbulence model. Among the other turbulence models available to the FLUENT user are the *standard* and the *realizable*  $k-\epsilon$  models.

As noted earlier, the standard model of Launder and Spalding preceded the RNG formulation, and is probably one of the most widely applied models in use. However, it relies on experimental observation for determining several of its constants, rather than their analytical derivation as with the RNG model, and it also lacks the additional terms in the transport equations for computing turbulent flows with swirl. The realizable  $k-\epsilon$  model developed by Shih, differs from the standard  $k-\epsilon$  model in two respects. First, it enforces certain mathematical constraints on the normal fluid stresses, consistent with the physics of turbulent flows. (The standard and RNG models, under some circumstances, may violate these constraints, and in this sense are “non-realizable.”) It does so by allowing the constant  $C_\mu$  in the standard model to

be a function of both the mean flow deformation and the turbulence. Secondly, it introduces a new transport equation for the rate of turbulent dissipation,  $\epsilon$ . Because of its relatively recent introduction, it is not yet clear under which circumstances this model is preferable to the RNG model.

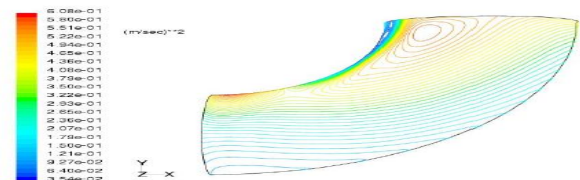


Fig. 14 Contours of Turbulent Kinetic Energy on Pipe Elbow Wall, top view

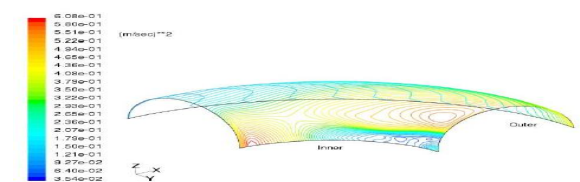


Fig 14. Contours of Turbulent Kinetic Energy on Pipe Elbow Wall, inside view (concluded)

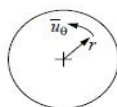
Solutions were generated using these two alternative turbulence models to see whether the flow features changed significantly when compared to the baseline predictions above using the RNG model. All other aspects of the simulations were kept the same, including the use of non equilibrium wall functions. The solution obtained using the standard  $k-\epsilon$  model is very similar to that with the RNG model, and for that reason will not be shown here. In particular, the wall shear stress (Fig. 9) still exhibits its maximum value on the inner radius, near the elbow entrance, as does the turbulent kinetic energy (Fig. 14); their magnitudes differed only by ~ 7% and 6%, respectively, between the two sets of calculations.

The calculations using the realizable  $k-\epsilon$  model exhibit greater discrepancies. Fig. 15 displays the predicted contours of wall shear stress for this case. When compared to Fig. 9, the most noticeable difference is that the maximum now appears on the outer radius, near the end of the elbow section, and is approximately 11% greater in magnitude than that in the earlier calculation. This is likely the result of the higher axial-velocity flow hugging the outer wall in this vicinity (cf. Fig. 13). A secondary maximum still appears on the inner radius just downstream of the entrance. Contours of the turbulent kinetic energy are shown in Fig. 16. Again, the maximum in this quantity shifts from the inner radius near the entrance in Fig. 14 to the outer radius near the exit, and is ~ 14% greater in magnitude.

These comparisons give some idea of the degree to which the choice of turbulence model affects the resulting predictions. However, absent any experimental flow field data, it is impossible to say which of the turbulence models does a better job of simulating actual conditions in the pipe elbow.

**Influence of Pressure Outlet Boundary Condition**

As was noted in §3.3, a PRESSURE OUTLET boundary condition is used to represent the outflow from the model at  $y = 400$  mm in Fig. 4.1. FLUENT gives the user two different options as to how the specified static gauge pressure at such a boundary, 19 bar in this case, is used in the calculations. The simplest choice is to impose the specified pressure uniformly over the entire cross section. Alternatively, one can use the so-called radial equilibrium pressure distribution option. If the cross-sectional flow were one of pure rotation about the center of the pipe, then the radial pressure gradient would be related to the tangential velocity component,  $\bar{u}_\theta$ , as follows,



$$\frac{\partial \bar{P}}{\partial r} = \frac{\rho \bar{u}_\theta^2}{r} \tag{12}$$

where  $\rho$  is the fluid density. The radial equilibrium pressure distribution option imposes the specified value at the minimum radius (the probe radius in this case), and then integrates Eq. (12) to get  $\bar{P}$  everywhere else in the cross section. This was used for the baseline calculations to account for the effects of any residual secondary flow remaining at the outlet from the model.

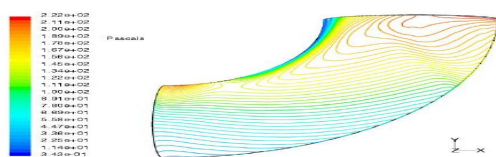


Fig. 15. Contours of Wall Shear Stress on Pipe Elbow Using Realizable  $k-\epsilon$

Turbulence Model, top view

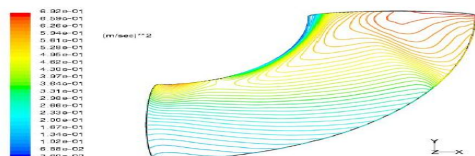


Fig. 16. Contours of Turbulent Kinetic Energy on Pipe Elbow Wall Using

Realizable  $k-\epsilon$  Turbulence Model, top view

To eliminate the possibility that the use of the radial equilibrium pressure distribution at the outlet was unduly influencing the flow in the elbow, the baseline calculation was repeated with this option turned off. That is, a uniform static gauge pressure of 19 bar was imposed at the outlet. As expected, the flowfield in the vicinity of the elbow predicted by this simulation was virtually indistinguishable from that in the baseline calculation. The effects of such a change are confined largely to the flow field adjacent to the outlet

**Influence of Sensor and Support**

It was decided to explore the degree to which the downstream sensor and associated support bracket might be influencing the flow in the elbow. Another simulation was performed using identical input parameters to those in the baseline calculations above—*i.e.*, with the RNG  $k-\epsilon$  turbulence model and radial equilibrium assumed for the outlet pressure boundary condition— except that the sensor and bracket were removed from the model geometry. The straight section of pipe that had previously contained these features was remeshed accordingly. The results of this simulation, not shown here, were in all respects very similar to the results presented in Figs. 6-14. In particular, the locations of both the maximum wall shear stress and the maximum turbulent kinetic energy were still on the inner radius just downstream of the entrance to the elbow. Their magnitudes were very close to those previously predicted as well. It was thus concluded that the presence of the sensor and bracket have a negligible impact on the flow in the immediate vicinity of the elbow.

This is not to say, however, that they do not have an influence on the flow field as a whole. The sensor and bracket together obstruct approximately 30% of the cross-sectional area that would otherwise be available to the flow (*cf.* Fig. 2). This is a significant blockage, and the flow pattern in the straight downstream section of pipe (not shown here) is very complex as a result of the wake shed by the support as well as the viscous boundary layer on the sensor itself.

This manifests itself in the much higher pressure drop that is predicted when the sensor and bracket are present, as compared to when they are not. Table 1 below summarizes the differences between the cross-sectionally-averaged pressures calculated at the inlet,  $\bar{P}_{in}$ , the beginning of the elbow,  $\bar{P}_{beg}$ , the end of the elbow,  $\bar{P}_{end}$ , and the outlet,  $\bar{P}_{out}$ . It is seen that the pressure losses across the straight upstream section of pipe and the elbow are virtually the same with and without the sensor present. But there is more than a ten-fold increase in the pressure drop across the straight downstream section, and a three-fold increase in the overall pressure drop between inlet

and outlet, when the sensor is inserted. So while the sensor has a negligible influence on the flow in the elbow itself, it has a major influence on the losses in the straight downstream pipe section, and the overall pressure loss. This also suggests that the straight section downstream of the elbow is sufficiently long so that the model's failure to include the tee section is unlikely to have much influence on the flow.

The above simulations specify the mass flow rate by using a VELOCITY-INLET boundary condition, and let the solution determine the overall pressure drop. The flow could also have been modelled by specifying the pressure drop between inlet and outlet, in which case the mass flow rate would have been determined as part of the solution. In the latter case, the presence of the sensor and associated bracket would have manifested itself in a reduced flow rate for the given pressure drop.

Table 1. Pressure Losses with and without Chemical Sensor, Pascals

	$P_{in} - P_{beg}$	$P_{beg} - P_{end}$	$P_{end} - P_{out}$	$P_{in} - P_{out}$
With Sensor	1686	3734	15188	20608
Without Sensor	1688	3728	1466	6882

## V. SUMMARY & CONCLUSIONS

Computational Fluid Dynamic (CFD) simulations of flow in a pipe elbow have been carried out using the FLUENT software for the purpose of trying to understand phenomena that relate to the process of flow-accelerated corrosion and erosion. The following specific conclusions have been drawn:

1. The qualitative features of the predicted flow field are all in agreement with the available literature. The simulation's predicted value for the diametrical pressure coefficient defined by Eq. (8) is in reasonable quantitative agreement with a published correlation based on experimental data. This gives us some confidence in the validity of the numerical results.
2. Our intuition led us to believe that the maximum corrosion/erosion, though not itself modelled in these simulations, would occur on the outside radius of the bend, and that its location would correlate with that of the maximum wall shear stress. However, the simulations indicate that the maximum wall shear occurs on the inside radius, just downstream of the entrance to the elbow.
3. We considered the possibility that some other fluid mechanical phenomenon, such as turbulence, could also be responsible for the corrosion. However, a plot of turbulent kinetic energy, Eq. (3), at the wall

reveals that its maximum also occurs on the inside radius, just downstream of the elbow entrance.

4. The above conclusions are based on the baseline simulation, which employed the RNG  $k-\epsilon$  turbulence model. To assess to what extent the choice of turbulence model may have influenced the results, simulations were also performed using the standard  $k-\epsilon$  and realizable  $k-\epsilon$  models. The simulation results obtained with the standard and RNG models were very similar.

Those from the realizable  $k-\epsilon$  model produced more significant differences. The maximums in both wall shear stress and turbulent kinetic energy now appear on the outer radius, near the elbow exit, and are ~11% and 14% greater, respectively, than those predicted in the baseline calculation; secondary maxima in both quantities still occur near the elbow entrance on the inner radius. Which set of results better reflects reality must await experimental corroboration.

5. Whether or not FLUENT's radial equilibrium pressure distribution option was used in the PRESSURE OUTLET boundary condition had no significant impact on the flow field near the elbow.
6. Simulations performed with and without the presence of the chemical sensor and its associated support bracket demonstrate that they have a negligible influence on the flow in the vicinity of the elbow. The fact that the maxima in wall shear stress and turbulent kinetic energy occur on the inner radius is therefore not an artifact of having introduced the sensor into the flow.
7. The principal effect of the sensor and its support bracket is to greatly increase the pressure loss in the straight section of pipe downstream of the elbow, as expected.

Lacking direct experimental evidence of where the corrosion/erosion is most severe, or data on the spatial variation of the wall shear stress, it is difficult to draw any final conclusions about the fidelity of these simulations. It would seem that one of two possibilities remain: either a) the maximum corrosion/erosion should be expected along the inner radius of the pipe, not the outer radius as was anticipated; or, b) if corrosion is found predominantly on the outer radius, some mechanism other than the purely fluid-mechanical scouring of the pipe surface is responsible. It is recommended that experimental data on the distribution of wall shear stress in the elbow be obtained, to facilitate comparisons with both the position of maximum

corrosion/erosion and the CFD simulations. If the location of maximum corrosion does not correlate with that of the wall shear, that would indicate that further work remains to be done on the corrosion/erosion model. If the two show good correlation with one another, but not with the CFD simulations, then modification of the fluid dynamic model would be in order.

With regard to the latter point, it should be noted that a grid-convergence study was not performed. The finite-volume method used by FLUENT approximates the PDEs describing the fluid motion as a system of algebraic equations derived by breaking the fluid continuum into a collection of discrete cells. The solution of this system should approach that of the original PDEs as the typical cell volume approaches zero. A grid-convergence study verifies this by simulating the same problem using progressively finer grids, *e.g.*, by halving the dimensions of each cell at least once, and preferably twice, and ascertaining whether the quantities of interest are asymptoting towards a solution that is independent of cell size. This can be an expensive undertaking. First, it requires generating the additional grids. Secondly, since those grids will have many more cells in them, the run time will increase dramatically owing to the fact that each iteration of the entire field will require more time, compounded by the fact that more iterations will be required to achieve a converged solution. For this reason, effort was focussed instead on gauging the influence of those aspects of the simulation — *i.e.*, turbulence model, form of the downstream boundary condition, and the presence or absence of the chemical sensor, that could be easily studied with the existing grid. Though the baseline grid is judged to be sufficiently refined for present purposes, should quantitative flowfield data become available for comparison, the time necessary to do such a grid-convergence study is probably warranted.

It is also possible we have been too quick to assume that the flow in the pipe is of only liquid form. Our understanding is that the water in nuclear plant piping networks is far from pure, being contaminated with dirt and other particulate matter. Depending on the size and mass of the particles, their inertia will tend to displace them toward the outside radius of the elbow, where mechanical impact with the surface could conceivably contribute to corrosion and erosion. FLUENT has the capability of modeling such particle-laden flows, as well as the resulting erosion of the surface. However, any such predictions would require knowledge of the number, size, and mass distributions of the particles themselves.

Results presented here employing the two most widely used turbulence models indicate that the greatest corrosion/erosion can be expected on the inner elbow radius, a

somewhat unexpected finding. The current round of KAERI experiments should determine whether that is indeed the case. At that point a decision can be made as to whether further measurements are needed to validate the simulations, and whether the CFD model needs to be improved, including the possibility of incorporating other phenomena.

## REFERENCES

- [1] Yakhot, V. and Orszag, S. A., “Renormalization Group Analysis of Turbulence: I. Basic Theory,” *Journal of Scientific Computing*, Vol. 1, No. 1, pp. 1-51, 1986.
- [2] Shih, T.-H., Liou, W. W., Shabbir, A., and Zhu, J., “A New k-ε Eddy-Viscosity Model for High Reynolds Number Turbulent Flows—Model Development and Validation,” *Computer Fluids*, Vol. 24, No. 3, pp. 227-238, 1995.
- [3] L. Wang, D. Gao, and Y. Zhang, “Numerical simulation of turbulent flow of hydraulic oil through 90° circular sectional bend,” *Chinese Journal of Mechanical Engineering*, p. 3901, 2012.
- [4] Richard A “Simulation-Driven Design Optimization: A Case Study on a Double 900 Elbow Bend” *International Journal of Modeling and Optimization*, Vol. 4, No. 6, December 2014
- [5] W. Yang and B. T. Kuan, “Experimental investigation of dilute turbulent particulate flow inside a curved 90° bend,” *Chemical Engineering Science*, vol. 61, no. 11, 2006, pp. 3593-3601.
- [6] Elok A Devi “Paleofacies of Eocene Lower Ngimbang Source Rocks in Cepu Area, East Java Basin Based on Biomarkers and Carbon-13 Isotopes” *Recent Adv Petrochem Sci* 5(1): RAPSCI.MS.ID.555654 (2018)
- [7] YUSUF “Elbow Pipe Design Optimization Of Oil And Gas Pipeline System Owned By Joint Operating Body Pertamina-Petrochina East Java Job P-Pej Tuban Based On Reliability”
- [8] N Crawford “ A numerical investigation of the flow structures and losses for turbulent flow in 90° elbow bends” *First Published December 23, 2008 Research Article.*
- [9] Pengfei Wang “Numerical Investigation on Fluid Flow in a 90-Degree Curved Pipe with Large Curvature Ratio” *Mathematical Problems in Engineering*, Volume 2015, Article ID 548262.